Engineering Fracture Mechanics 199 (2018) 635–646

Contents lists available at ScienceDirect

Engineering Fracture Mechanics

journal homepage: www.elsevier.com/locate/engfracmech

Size-dependent damage and fracture of two-layer systems

L.H. Liang[a,c,*], H.Y. Liu[b], H. Long[a,c], Y.G. Wei[b]

[a] LNM, Institute of Mechanics, Chinese Academy of Sciences, Beijing 100190, China
[b] College of Engineering, Peking University, Beijing 100871, China
[c] University of Chinese Academy of Sciences, Beijing 101408, China

ARTICLE INFO

Keywords:
Damage
Fracture
Ceramic layers
Interface strength
Interface toughness

ABSTRACT

Two-dimensional three-point bending and four-point bending of two-layer finite element models for a ceramic layer on a metallic substrate are developed to study the damage and fracture characteristics of two-layer systems by introducing an interface cohesive zone model. The damage evolution and fracture modes of ceramic layers of different thicknesses, with loading on the metallic substrates, are compared under different loading conditions based on simulation results. Multiple surface cracks, vertical to the interface between the ceramic and metallic layers, appear in all ceramic layers under four-point bending loading and only in the thinner ceramic layers under three-point bending. For the thicker ceramic layer systems under three-point bending loading, the interface fracture between the ceramic and metallic layers is the main failure mode, agreeing with previous experimental observations. Damage and damage rate, defined by the simulated crack evolution, are found to obey a power law relation with loading and to be consistent with the theoretical predictions based on a mathematical damage model. The damage coefficient, a parameter reflecting the damage rate, is found to be size-dependent based on the simulation and experimental results, and its energy mechanism is discussed. The damage is slower for the thinner ceramic layers with a smaller damage coefficient than that for the thick ceramic layers under three-point and four-point bending loading, and the damage of the ceramic layer systems is faster under three-point bending than under four-point bending, resulted from different crack distributions, damage localization degrees, and energy dissipation. Moreover, the damage is slower for the nanostructured ceramic layers with the stronger interface strength or toughness between two layers.

1. Introduction

Multi-layer structures with heterogeneous materials are widely used in many fields, such as electronic integrated circuits, batteries, thermal barrier coatings, and thermal electric fields. These structures are usually related to the metal–semiconductor or metal–ceramic interface, and the interface fracture between two layers and the surface fracture of thin films or coatings on substrates play an important role in affecting the properties of the entire structure. Therefore, damage and fracturing of two-layer interface systems are attracting great attention [1–3]. Theoretical studies of crack distribution in thin films or coatings have been carried out for approximately 30 years [4]. An analytic solution for crack spacing in brittle films, under a uniform tensile stress, on elastic substrates was developed based on the fracture mechanics [4]. The fracture behavior of brittle film/ductile substrate systems with uniaxial tensile strain was studied by developing an elastic–plastic shear–lag model, and the crack density was calculated as a function of strain [5]. An energy model of segmentation cracking of thin films based on a delamination model was also developed,

* Corresponding author at: Institute of Mechanics, Chinese Academy of Sciences, Beijing 100190, China.
E-mail address: lianglh@lnm.imech.ac.cn (L.H. Liang).

https://doi.org/10.1016/j.engfracmech.2018.06.040
Received 15 May 2018; Received in revised form 25 June 2018; Accepted 26 June 2018
Available online 30 June 2018

and the crack number in brittle thin films on a ductile substrate was predicted [6]. With the development of experimental studies, the crack evolution in coatings was also captured by in situ scanning electron microscopy [7], a digital image correlation technology, acoustic emission monitoring [8,9], etc. The interface toughness of multilayered systems, related to interface cracking, was measured by developing bending tests and combined with an energy approach [10]. Numerical studies were carried out to understand the cracking behavior and failure mechanism of coatings under thermal loading [11,12]. Damage of coatings under thermal loading was characterized by an advanced experimental method [13] or numerical method [14].

In recent experiments, different fracture modes of ceramic coatings with different thicknesses on the same alloy substrates under three-point bending loading were found [7], and different crack densities in the ceramic coatings with different thicknesses under four-point bending loading were also reported [15]. Moreover, the damage based on crack evolution was described well by a power law damage model [16,17]. In the damage model, the damage coefficient, as a parameter reflecting damage rate, was proposed by mathematical derivation and determined by the experimental results of initial and complete damage variables and the controlling variables [17]. The results show the damage coefficient seems to be different for ceramic coatings with different thicknesses or under different loading, and its mechanism is unclear. To understand the experimental phenomenon better and the physical meaning of the damage coefficient, a systematic finite element simulation to study damage and fracture behavior of two-layer systems with different ceramic layer thicknesses under different loading conditions is carried out. The size effect and related energy mechanism of the damage coefficient are analyzed and discussed.

2. Finite element models

2.1. Bending models of two-layer systems

Two two-dimensional numerical models for three-point and four-point bending were built with the commercially available finite element code ABAQUS. Both models include two layers, a ceramic layer of several hundreds of microns and a metallic layer of 1.2 mm, as shown in Figs. 1 and 2, respectively. The lengths used in the three-point and four-point bending models were 16 and 24 mm, respectively, and a series of thicknesses of 100, 200, 300, 400, and 500 μm for the ceramic layers were used for both models. Two ends of the downside of the ceramic layers were simply supported, and the displacement load was applied on the upside of the metal layers.

Both layer sheets were meshed using the four-node plane strain elements, and the four-node interface cohesive elements were adopted between the neighbor segments of the ceramic layer and between the ceramic and the metallic layers, as shown in Figs. 1 and 2. The elastic modulus E_C and the Poisson's ratio ν_C were, respectively, 18 GPa and 0.2 for the ceramic layers [15,18]. The linear elastic constitutive relation was considered for the ceramic layers, and the elastoplastic constitutive model with linear hardening was considered for the metallic layers, as shown in Eq. (1),

$$\varepsilon = \begin{cases} \frac{\sigma}{E_S}, & \sigma \leqslant \sigma_Y \\ \frac{\sigma_Y}{E_S}\left(\frac{\sigma}{\sigma_Y}\right)^{1/n}, & \sigma > \sigma_Y \end{cases} \tag{1}$$

where $E_S = 200$ GPa, $\nu_S = 0.3$ for the metallic substrate layers [15,19], the yield stress $\sigma_Y = 800$ MPa, and the hardening power exponent $n = 0.2$ by fitting the experimental results [15]. Especially, the interface cohesive model is introduced in the interface elements between two layers and between the neighboring segments of the ceramic layers to study the interface fracture and crack evolution in brittle ceramic layers.

2.2. Cohesive zone model in interface elements

An interface cohesive zone model based on the traction–separation relations is suitable to describe the interface decohesion [20,21]. The bilinear traction–separation relation was adopted here for the interface elements between the neighboring segments of ceramic layers and between the ceramic layers and the metallic layers, as shown in Fig. 3. Fig. 3(a)–(c) show the cohesive relation in the mixed mode, the tension, and the shear directions, respectively.

For the pure tension mode (mode I), the cohesive relation is expressed as

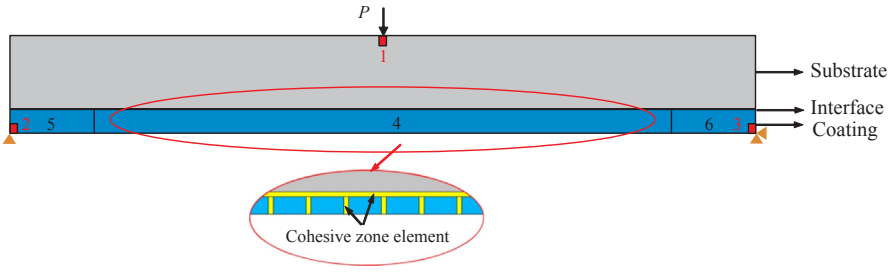

Fig. 1. Schematic of three-point bending model.

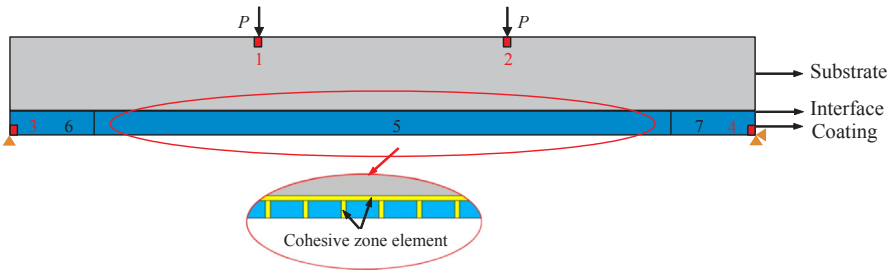

Fig. 2. Schematic of four-point bending model with a span length of 8 mm.

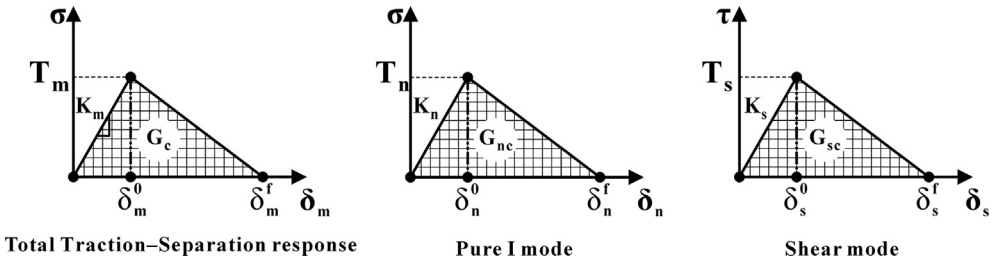

Fig. 3. Schematic of interface cohesive model in (a) mixed, (b) tension, and (c) shear modes, respectively.

$$\sigma = \begin{cases} T_{\mathrm{n}} \dfrac{\delta_{\mathrm{n}}}{\delta_{\mathrm{n}}^{0}}, & \delta_{\mathrm{n}} \leqslant \delta_{\mathrm{n}}^{0} \\ T_{\mathrm{n}} \dfrac{\delta_{\mathrm{n}}^{\mathrm{f}} - \delta_{\mathrm{n}}}{\delta_{\mathrm{n}}^{\mathrm{f}} - \delta_{\mathrm{n}}^{0}}, & \delta_{\mathrm{n}} \geqslant \delta_{\mathrm{n}}^{0} \end{cases} \quad \text{(normal direction)} \tag{2}$$

when the normal separating displacement $\delta_{\mathrm{n}} > 0$, where σ represents normal separating stress, and T represents the maximum separating stress (i.e., interface strength), the subscript n represents the pure tensile direction, and the superscripts 0 and f represent the critical displacement corresponding to the strength T and the fracture displacement corresponding to the complete interface failure, respectively. For pure shear mode, a similar cohesive relation is assumed, and τ represents tangent separating stress, and the subscript s represents the pure shear direction. When $\delta_{\mathrm{n}} < 0$, only the tangent stress is effective. The critical fracture energy G_{nc} in the normal direction is

$$G_{\mathrm{nc}} = \int_{0}^{\delta_{\mathrm{n}}^{\mathrm{f}}} \sigma \mathrm{d}\delta_{\mathrm{n}} = \frac{1}{2} T_{\mathrm{n}} \delta_{\mathrm{n}}^{\mathrm{f}} \tag{3}$$

and the critical fracture energy G_{sc} in the tangent direction has similar form.

As the load increases beyond a critical value, the interface is in a damaged state. The damage initiates when a certain criterion is satisfied. For the mixed mode, the maximum stress criterion is adopted to characterize the interfacial damage [7], which is described as

$$\mathrm{MAX}\left\{\frac{\langle \sigma \rangle}{T_{\mathrm{n}}}, \frac{\tau}{T_{\mathrm{s}}}\right\} = 1 \tag{4}$$

where $\langle\rangle$ represents the Macaulay bracket defined by $\langle x \rangle = (|x| + x)/2$ with the usual interpretation that a pure compressive deformation or stress state does not initiate damage. It is assumed that interfacial damage occurs when Eq. (4) is satisfied, and a single damage variable D_{i} based on the total displacement δ_{m} of the mixed mode is introduced ($\delta_{\mathrm{m}} = \sqrt{\delta_{\mathrm{n}}^{2} + \delta_{\mathrm{s}}^{2}}$) [7,22] as

$$D_{\mathrm{i}} = \begin{cases} 0, & \delta_{\mathrm{m}} \leqslant \delta_{\mathrm{m}}^{0} \\ \dfrac{\delta_{\mathrm{m}}^{\mathrm{f}}(\delta_{\mathrm{m}} - \delta_{\mathrm{m}}^{0})}{\delta_{\mathrm{m}}(\delta_{\mathrm{m}}^{\mathrm{f}} - \delta_{\mathrm{m}}^{0})}, & \delta_{\mathrm{m}}^{0} < \delta_{\mathrm{m}} < \delta_{\mathrm{m}}^{\mathrm{f}} \\ 1, & \delta_{\mathrm{m}} \geqslant \delta_{\mathrm{m}}^{\mathrm{f}} \end{cases} \tag{5}$$

The interface fracture energy can be regarded as the mixed-mode fracture energy, and the power exponential criterion [7,23] is employed to describe the mixed-mode fracture,

$$\frac{G_{\mathrm{n}}}{G_{\mathrm{nc}}} + \frac{G_{\mathrm{s}}}{G_{\mathrm{sc}}} = 1 \tag{6}$$

where G_{n} and G_{s} represent the work done by the traction in the tension and the shear directions, respectively. The total critical fracture energy can be determined by $G_{\mathrm{c}} = G_{\mathrm{n}} + G_{\mathrm{s}}$ when Eq. (6) is satisfied.

For the cohesive elements between the ceramic layer segments, $T_{\mathrm{n}} = 80$ MPa and $T_{\mathrm{s}} = 200$ MPa are taken referring to the

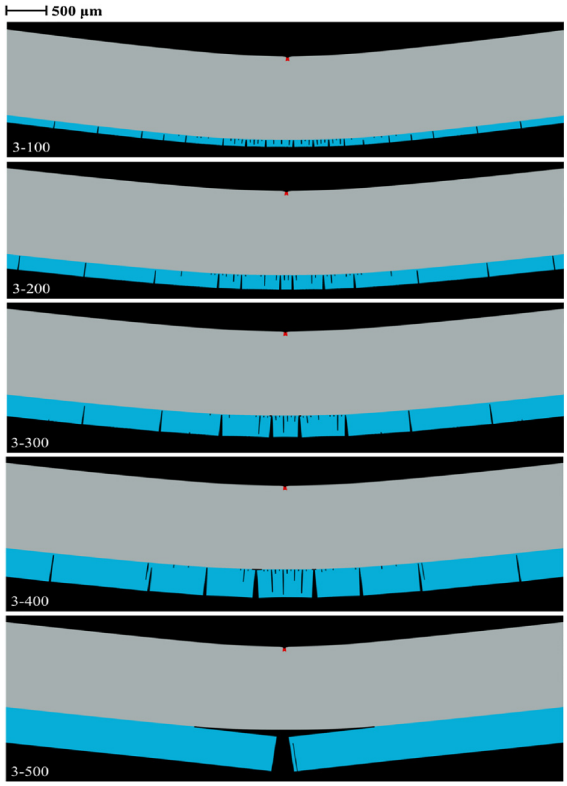

Fig. 4. Simulation results of three-point bending model with a series of ceramic layer thicknesses (100–500 μm) at a displacement of 1 mm, where map 3–100 denotes a 100 μm ceramic layer under three-point bending and similar notes for other maps.

experimental results [15], and $G_{nc} = 20\ J/m^2$ and $G_{sc} = 40\ J/m^2$ are adopted. For the cohesive elements between the ceramic layers and the metallic layers, $T_n = 200$ MPa and $T_s = 40$ MPa are taken, and $G_{nc} = 400\ J/m^2$ and $G_{sc} = 200\ J/m^2$ are adopted referring to the related literature about the thermal barrier coatings [24]. The stiffness K in the interface cohesive model is the slope of the initial segment of the traction–separation curve and is taken to satisfy the relation of $\delta^f/\delta^0 = 4$ [7].

3. Simulations result of fracture modes of two-layer systems

Fig. 4 shows the fracture modes of the two-layer systems under three-point bending loading. The multiple transverse cracks, vertical to the interface between the ceramic layers and the metallic layers, are the main fracture mode for the thinner ceramic layer samples with layer thickness of about 100–400 μm (corresponding to the maps from 3 to 100 to 3–400 μm in Fig. 4), and tensile failure dominates the thinner ceramic layers, which had been analyzed in the previous stress study on similar experimental phenomena [7]. The interface fracture is the main fracture mode for the thicker ceramic layer samples with layer thickness of about 500 μm (map 3–500 in Fig. 4), and the interface shear failure dominates the thicker ceramic layer systems. The simulation results are similar to the previous experimental results of ceramic coatings bonded on the alloy substrates [7].

Fig. 5 shows the fracture modes of the two-layer systems under four-point bending loading. The multiple transverse cracks and the tensile strength failure dominate for both the thinner and the thicker ceramic layers under four-point bending. The crack density in the thinner ceramic layers (map 4–100 in Fig. 5) is larger than that in the thicker ceramic layers (map 4–500 in Fig. 5). The simulation results are also consistent with the previous experimental results [15].

4. Damage characterization of crack evolution

4.1. Damage definition

The load-displacement curves based on the four-point bending and three-point bending simulations are shown in Figs. 6(a) and 7(a), respectively. The figures show that the curves include two steps: a linear step and a nonlinear step. The initial nonlinear step is considered as a damage step of the ceramic layers. At the beginning of the nonlinear step of the load–displacement curve of a system with a ceramic layer of 400 μm under four-point bending loading, as shown in Fig. 6(a) (point 1), two transverse cracks in the ceramic layers initiate abruptly from the surface of the layers due to enough large tensile stress, as shown in Fig. 6(b) (map 4–400-1 corresponding to point 1 in (a)), which is defined as the initial damage. Then, more cracks emerge and go through the ceramic layer

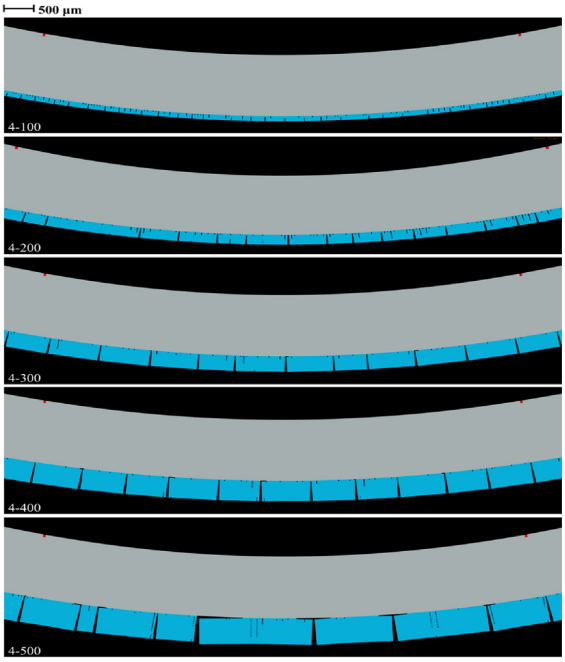

Fig. 5. Simulation results of four-point bending model with a series of ceramic layer thicknesses at a displacement of 1 mm, where map 4–100 denotes a 100 μm ceramic layer under four-point bending and similar notes for other maps.

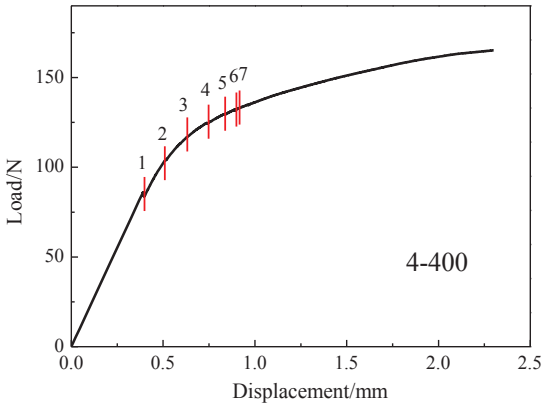

Fig. 6. (a) Load–displacement curve of the system with a 400 μm ceramic layer under four-point bending; (b) Crack evolution corresponding to points 1, 3, and 7 in the load–displacement curve in (a).

rapidly with loading as shown in Fig. 6(b) (map 4–400-3 corresponding to point 3 in (a)). When the main transverse cracks in the pure bending section saturate (map 4–400-7 in Fig. 6(b)), the saturation point is defined as the complete damage corresponding to point 7 in Fig. 6(a). The step from the imitation of transverse cracking to the saturation is the damage step, as shown in Fig. 6(a), which is used to describe the damage by capturing the total crack length evolution in the pure bending section. For the systems with thinner ceramic layers under three-point bending loading, similar crack evolution behavior is found, and the same damage is defined, because the same tensile failure dominates in these ceramic layers.

For the thicker ceramic layer system (e.g., 500 μm ceramic layer) under three-point bending loading, the interface crack evolution between the ceramic layer and the metallic layer, as shown in Fig. 7(b), is used to describe the damage, because the interface shear is the main failure mode. The initial damage is defined based on the initial interface crack length (map 3–500-1 in Fig. 7(b)), and the complete damage is considered at point 4 in Fig. 7(a) (corresponding to map 3–500-4 in Fig. 7(b)) by comparing the experimental results of the failure point of the ceramic coatings, at which the slope of the curve increases due to the contribution from the alloy substrate [25].

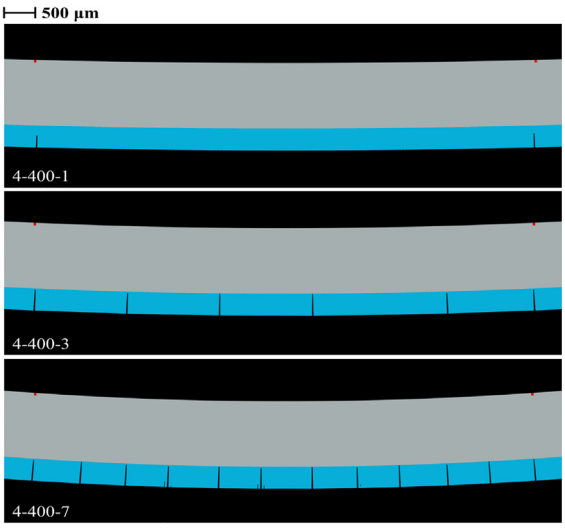

Fig. 6. (*continued*)

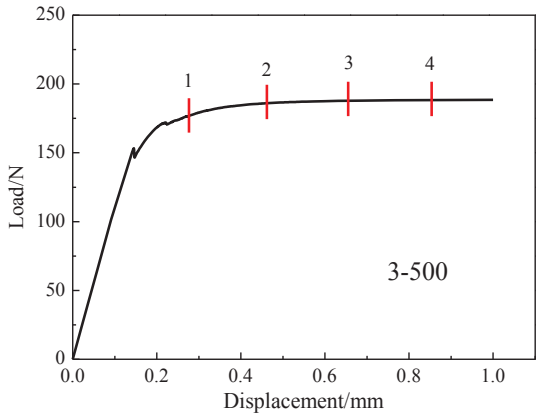

Fig. 7. (a) Load–displacement curve of the system with a 500 μm ceramic layer under three-point bending; (b) Crack evolution corresponding to points 1–4 in the load–displacement curve in (a).

4.2. Review of the mathematical damage model

Considering a controlling variable λ of one system is continuous and derivative for damage evolution of the system before its catastrophic rupture, it can be expressed as the Taylor expansion of the damage D,

$$\lambda = \lambda_f + \lambda'(D_f) \times (D - D_f) + \frac{\lambda''}{2}(D_f) \times (D - D_f)^2 + o(D - D_f)^2 \tag{7}$$

where the damage variable D is calculated based on the transverse crack or interface crack length [17], which is the damage of the whole ceramic layer system, different from that of each interface element defined in Eq. (5), and the controlling variable is the corresponding tensile or shear stress for transverse cracking or interface cracking, which can be calculated by the load based on the composite beam model [7]. D_f represents the complete damage corresponding to the failure stress λ_f, the damage and the controlling variables are both normalized here, and D_f and λ_f are both equal to 1. $\lambda'(D_f)$ and $\lambda''(D_f)$ represent the first-order and the second-order derivation at the failure point.

The fracture of brittle materials possesses catastrophic failure characteristics, and the damage rate tends to be infinite at the failure point [16,17,25,26], i.e., $\lim_{\lambda \to \lambda_f} = \frac{dD(\lambda)}{d\lambda} = \infty$ and $\lim_{D \to D_f} = \frac{d\lambda(D)}{dD} = 0$. Neglecting the high-order term (higher than second-order) and combining with $\lim_{D \to D_f} = \frac{d\lambda(D)}{dD} = 0$, Eq. (7) becomes

$$D = 1 - C(1 - \lambda)^{1/2} \tag{8}$$

where $C = [-\lambda''(D_f)/2]^{-0.5}$ is the damage coefficient. For example, for the ceramic layers dominated by tensile failure, when the tensile stress σ in the ceramic layers reaches a certain value $\sigma = \sigma_0$, the damage initiates $D = D_0$ [17]. Note that the initial damage $D_0 = L_0/L_f$ of one system is defined by a ratio of the initial crack length L_0 (the corresponding stress is σ_0) to failure crack length L_f

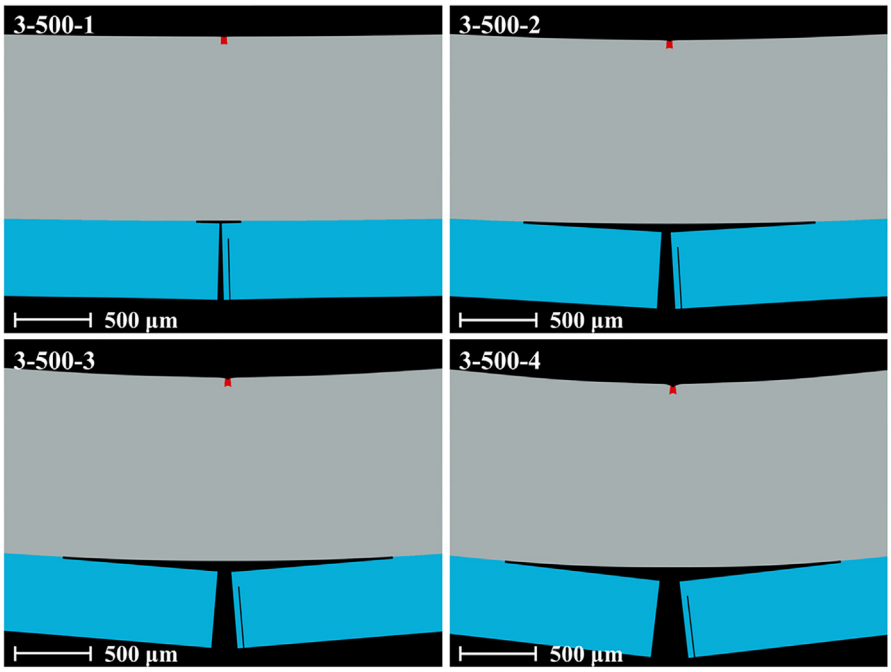

Fig. 7. (*continued*)

(the corresponding stress is σ_f), and the corresponding normalized stress is $\lambda_0 = \sigma_0/\sigma_f$ (or τ_0/τ_f for interface shear failure). Taking them into Eq. (8), the damage coefficient

$$C = (1-D_0)/(1-\lambda_0)^{0.5} \tag{9}$$

can be obtained. Eq. (8) shows that the evolution of damage with the controlling variable obeys the power-law relation with the exponent of 1/2. The damage D equals 1 when the controlling variable λ reaches 1.

Furthermore, the damage rate of the coatings can be written as

$$R = \frac{\mathrm{d}D}{\mathrm{d}} = \frac{C}{2}(1-\lambda)^{-1/2} \tag{10}$$

Eq. (10) shows the power-law singularity of the damage rate at the failure point, which agrees with the power-law relation of rock catastrophic rupture [16]. Taking the natural logarithm for the two sides of Eq. (10), the following expression can be obtained,

$$\ln R = \ln\left(\frac{C}{2}\right) - 0.5\ln(1-\lambda) \tag{11}$$

Note that the damage model has been validated by experimental results [17].

4.3. Comparison between simulation results and the damage model

Figs. 8 and 9, respectively, show the damage and damage rate of two-layer systems under three-point bending loading, the symbols are the simulation results and the lines are the theoretical predictions based on Eqs. (8) and (10), respectively. Fig. 10 shows the natural logarithm of the damage rate, where the lines are the average values of the simulation results based on Eq. (11). The figures show that the simulation results are consistent with the model's predictions. The damage increases with increasing load and is complete when the controlling load reaches the failure point, as shown in Fig. 8. Fig. 9 shows that the damage rate increases rapidly when the controlling load is close to the failure point, and it shows the power-law singularity at the failure point. The damage coefficient calculated based on Eq. (9) with D_0 and λ_0 resulting from the simulated results, varies from about 1.2 to 2.8, as shown in Table 1. The damage coefficient of the thicker ceramic layer system (500 μm) is obviously larger than that of the thinner ceramic layers, which agrees with previous experimental results of the ceramic coating samples [17]. The difference of the damage coefficient between the thicker and thinner ceramic layer systems can also be found in Fig. 10. It is caused by different failure modes.

Figs. 11 and 12, respectively, show the damage and damage rate of two-layer systems under four-point bending loading. Fig. 13 shows the natural logarithm of the damage rate. The figures show that the simulation results are consistent with the model's predictions. The damage coefficient based on the simulated results varies from 1.2 to 1.45, as shown in Table 2, which is also consistent with previous experimental results [15]. The damage coefficient of the thicker ceramic layers is larger than that of the thinner ceramic layers, although the difference is small due to the same failure mode. Comparing Table 2 with Table 1, the average damage coefficient of 1.34 under four-point loading is smaller than the average value of 1.58 under three-point bending loading, because the

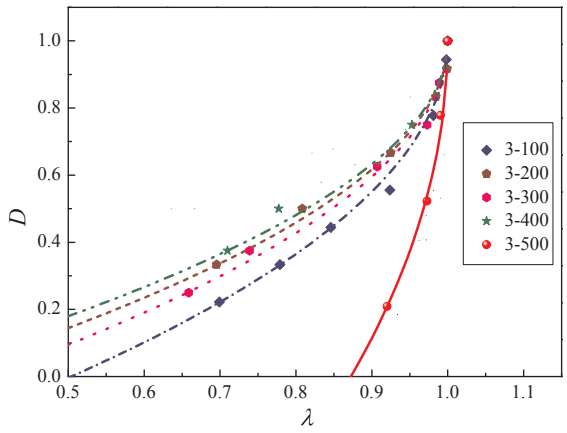

Fig. 8. Damage of the systems versus controlling stress under three-point bending loading.

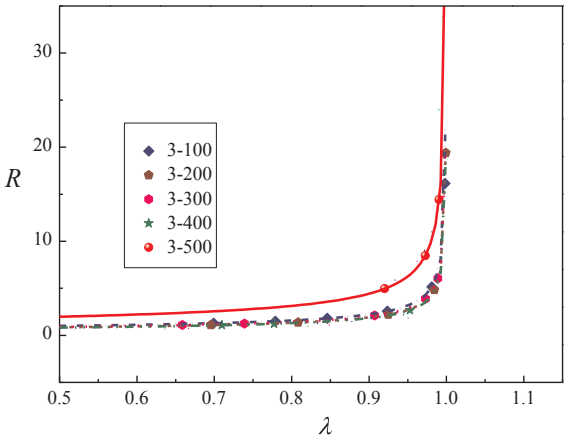

Fig. 9. Damage rate of the systems versus controlling stress under three-point bending loading.

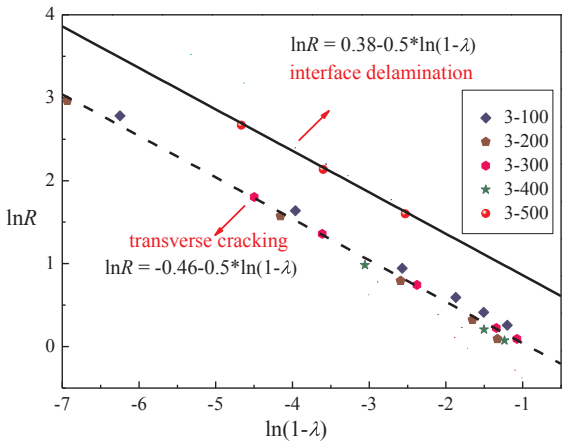

Fig. 10. Logarithm of damage rate of the systems under three-point bending loading.

damage for transverse cracking of the ceramic layers in pure bending sections is slower, and the damage for interface cracking between the thick ceramic layer and the metallic layer under three-point bending is faster.

5. Discussion of energy related to damage coefficient

According to Eq. (10), the damage coefficient C is related to the speed of the damage, the larger C corresponds to the larger

Table 1
Damage coefficient C of two-layer systems under three-point bending loading.

Ceramic layer thickness (μm)	100	200	300	400	500
C resulting from the present simulations	1.42	1.23	1.3	1.15	2.8
C resulting from the previous experiments [17]	1.21				1.78

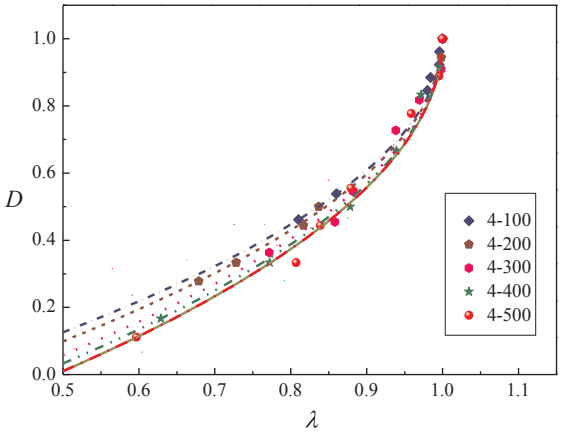

Fig. 11. Damage of the ceramic layers versus tensile stress under four-point bending loading.

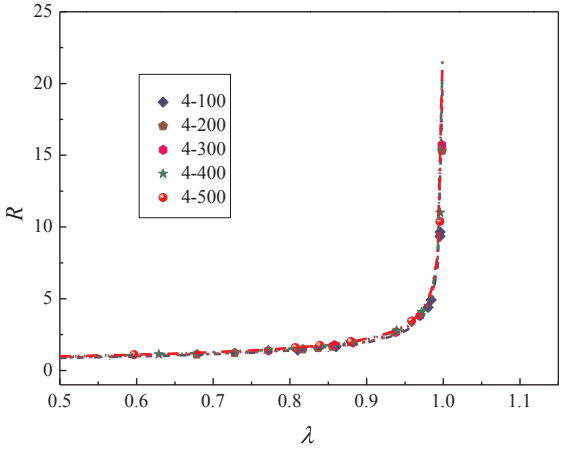

Fig. 12. Damage rate of the ceramic layers versus tensile stress under four-point bending loading.

damage rate R, and C is determined by the failure strength σ_f of the systems and the initial damage D_0 and stress σ_0 as follows

$$C = \frac{1-D_0}{\sqrt{1-\sigma_0/\sigma_f}} \tag{12}$$

This is based on Eq. (9) combined with $\lambda_0 = \sigma_0/\sigma_f$ and is the same for interface shear failure with $\lambda_0 = \tau_0/\tau_f$. From the simulation, when one crack occurs and the damage initiates in the brittle layer, σ_0 should be larger than the interface strength T_m of cohesive elements, and the strain work should be larger than the critical fracture energy G_c. D_0, related to initial crack length, should be related to the number of fractured cohesive elements. For ideal homogeneous brittle media, σ_0 should be equal to σ_f, i.e., the tensile stress reaches the strength of the materials, multiple transverse cracks occur simultaneously, and the ceramic layers fail, which corresponds to the singularity of C and R. For real experimental samples as heterogeneous media, D_0 initiates at some microscale defects or microcracks. The initial damage stress σ_0 is always smaller than the failure stress σ_f of the entire layer. When σ_0 is closer to σ_f, which represents the faster rate from σ_0 to σ_f, C is larger, and the damage rate is larger. The smaller difference between σ_0 and σ_f can be reflected by the smaller $d\sigma/dN$, where N is the number of transverse cracks in the ceramic layer. When $\sigma = \sigma_f$, N saturates. The failure stress σ_f is related to the total energy release of the cracks at the failure point with the saturated crack density.

Considering the energy principle in the damage step of a ceramic layer, the total potential energy change U_t of the ceramic layer includes increased surface energy due to ceramic cracking and released elastic strain energy,

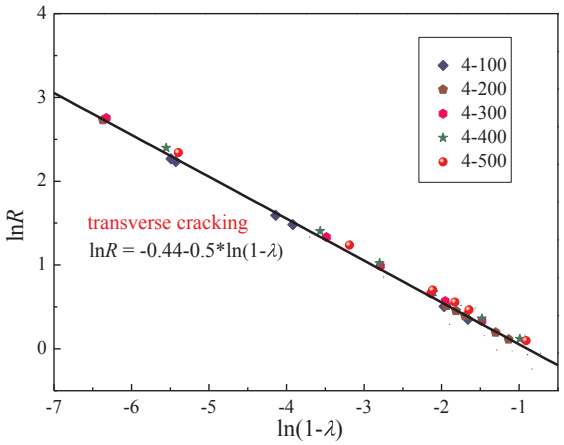

Fig. 13. Logarithm of damage rate of the ceramic layers under four-point bending loading.

Table 2
Damage coefficient C of ceramic layers under four-point bending loading.

Ceramic layer thickness (μm)	100	200	300	400	500
C resulting from the present simulations	1.2	1.3	1.4	1.35	1.45
C resulting from the previous experiments [15]	1.14			1.4	

$$U_t = U_s + U_e \tag{13}$$

where $U_s = 2N\gamma bh_C$ is the total surface energy due to the cracking with the crack number N in the ceramic layer, γ is the specific surface energy density of the ceramic, b is the layer width (equal to 1 in the simulation), h_C is the layer thickness considering that the cracks are through the layer. $U_e = -\frac{1}{2}bh_C d_a N\frac{\sigma^2}{E_C}$ is the total elastic strain energy with the average cracking distance d_a and the elastic modulus E_C of the ceramic layer. According to the energy variation principle, when the cracking is in a stable state,

$$\frac{dU_t}{dN} = 2bh_C\gamma - \frac{1}{2}bh_C d_a\frac{\sigma^2}{E_C} - \frac{1}{2}bh_C N d_a\frac{2\sigma}{E_C}\frac{d\sigma}{dN} = 0 \tag{14}$$

and thus

$$\frac{d\sigma}{dN} = \frac{2\gamma E_C}{Nd_a\sigma} - \frac{\sigma}{2N} = \frac{2\gamma E_C}{l\sigma} - \frac{\sigma}{2l}d_a \tag{15}$$

can be obtained by considering $Nd_a = l$ with the length of the pure bending section l. For the thicker ceramic layers, d_a is larger, as shown in Fig. 5. According to Eq. (15), $d\sigma/dN$ is smaller when σ is the same, since the other material parameters are constants, and thus C and R are larger, as discussed above, which agrees with the simulation and experimental results, as shown in Tables 1 and 2 (the larger C for thicker ceramic layers).

According to the energy balance principle, when $\sigma = \sigma_f$, $U_t = 0$,

$$\sigma_f = 2\sqrt{\gamma E_C/d_a} \tag{16}$$

can be obtained based on Eq. (13). Eq. (16) indicates that the failure stress of the ceramic layers is proportional to the surface energy density and elastic modulus of the ceramics, and inversely proportional to the average cracking distance. According to Eq. (16), the different cracking distances for the thinner and thicker ceramic layers, as shown in Fig. 5, correspond to different failure stresses, since the specific surface energy and the elastic modulus are constants as material parameters.

Furthermore, according to Eq. (12), the larger σ_f corresponds to the smaller C. Combined with Eqs. (12) and (16), C is approximately proportional to the crack distance $d^{0.25}$, i.e., d is smaller and C is smaller, which is consistent with the simulation and experimental results [15]. The transverse crack distance is smaller for the thinner ceramic layers, as shown in Fig. 5, and the damage coefficient is also smaller, as shown in Table 2. For example, for the experimental results shown in Table 2, $C2/C_1 = 1.4/1.14 = 1.23$, the subscripts 1 and 2 represent the results of 100 and 400 μm ceramic layers, respectively, and the corresponding crack distances are 0.23 and 0.86 mm, respectively [15], i.e., $(d_2/d_1)^{0.25} = (0.86/0.23)^{0.25} = 1.39$. The value is close to the ratio of the damage coefficient, which validates $C \propto d^{0.25}$.

For the same ceramic layer systems under three-point bending and four-point bending loading, respectively, the damage coefficients are also different, and the average damage coefficient under four-point bending is smaller than that under three-point bending, as discussed. For example, for the experimental results of ceramic layers of 100 μm, as shown in Tables 1 and 2, $C3/C_4 = 1.21/1.14 = 1.06$, where the subscripts 3 and 4 represent the results under three-point bending and four-point bending,

respectively, the corresponding crack distances are 0.28 [7] and 0.23 mm [15], respectively, i.e., $(d_3/d_4)^{0.25} = (0.28/0.23)^{0.25} = 1.05$, and the value is almost equal to the ratio of their damage coefficients. More cracks release greater strain energy, thus, the damage is slower for the thinner ceramic layers under four-point bending loading, whereas fewer cracks correspond to the more localized damage zone and the more obvious catastrophic failure. For the thicker ceramic layer system under three-point bending loading, one main interface crack between two layers, as shown in Fig. 4, is more localized than the multiple transverse cracks in the thinner ceramic layers, and thus the damage coefficient is obviously large, as shown in Table 1.

In the previous three-point bending experiments [17], the average damage coefficient of nanostructured thick ceramic coatings was found to be smaller than that of conventional microscale microstructured thick coatings in the interface cracking process between the coatings and the substrates, $C_m/C_n = 1.78/1.52 = 1.17$ [17], where the subscripts m and n represent the microscale microstructured and nanostructured ceramic layers, respectively. According to Eq. (12), C is approximately inversely proportional to $\sigma_f^{0.5}$; thus, the interface failure strength σ_{fn} of nanostructured layers should be larger than that of the conventional ones σ_{fm}, which has been validated by experiments [27]. The interface strength σ_f between the nanostructured ceramic coatings and the alloy substrates is larger than that between the conventional coatings and the same alloy substrates, $\sigma_{fn}/\sigma_{fm} = 1.86$ [27], and $(\sigma_{fn}/\sigma_{fm})^{0.5} = 1.36$ close to the ratio of their damage coefficients. The smaller damage rate of nanostructured layers may be related to the smaller microstructure scale and more microinterfaces, which leads to the weaker localization degree of damage. The relation between micro damage and macro failure has been studied, and the related energy dissipation was discussed [28]. According to Eqs. (3) and (16), the interface strength is proportional to critical fracture energy (i.e., fracture toughness) G_c, and the fracture toughness is inversely proportional to damage rate R (i.e., $R \propto f(k)/G_c$ with a function of slope k of the load–displacement curves) based on the mechanical damage model and energy analysis [25]; therefore, the damage coefficient is inversely proportional to the interface strength.

To check the effects of interface strength and fracture toughness, the corresponding numerical simulations were carried out further by changing the interface cohesive strength T_n and fracture toughness G_{nc}, as shown in Figs. 14 and 15, respectively, for the thicker ceramic layer systems with a given thickness ratio of a ceramic–metal two-layer system ($h_c/h_s = 0.4$) and the normalized strength and toughness. The symbols are simulation results and the lines are theoretical predictions based on Eq. (8). Although there are some differences between the simulation data and the theoretical predictions, as shown in Fig. 15, the change tendency of the damage coefficient with changing interface toughness is the same. The damage evolution becomes slow with increasing interface cohesive strength (Fig. 14) or fracture toughness (Fig. 15), i.e., the damage coefficient decreases, agreeing with the experimental results and above analysis. The effects of interface properties on the damage rate also reflect the parameter effects of cohesive elements at the same time. The relation between the local interface cohesive elements and the macro fracture of the whole system will be studied in detail in future work.

6. Conclusions

In summary, two two-layer finite element models under three-point bending and four-point bending loading were established by introducing an interface cohesive model, and the damage evolution and fracture characteristics of a brittle layer with different thicknesses and with different interface strengths were studied and compared. The damage coefficient, reflecting the damage rate of the cracking, was found to size dependent. The damage of the thinner ceramic layers was slower, and the damage of two–layer systems under four-point bending loading was also slower than that under three-point bending loading, which is explained by the different surface crack density distribution related to energy dissipation. The damage of the thicker ceramic layer systems under three-point bending loading was the fastest due to the different failure mode and the high damage localization degree of interface cracking. Moreover, the damage of nanostructured thick ceramic layers was slower than that of the conventional thick layers due to the stronger interface strength between the nanostructured ceramic layers and the metallic layers. The large interface fracture toughness also decreased the damage rate. The simulation results agree with the experimental results. The work is helpful to guide the design of related two-layer parts with brittle layers and provides a basis for decreasing catastrophic failures.

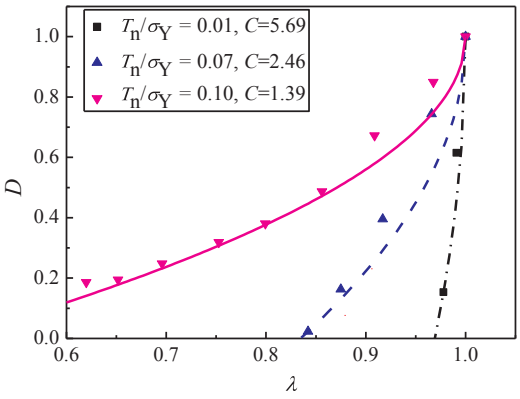

Fig. 14. Damage of two-layer systems with different interface strengths and same fracture toughness ($G_{nc}/(\sigma_Y h_s) = 3 \times 10^{-5}$) under three-point bending loading.

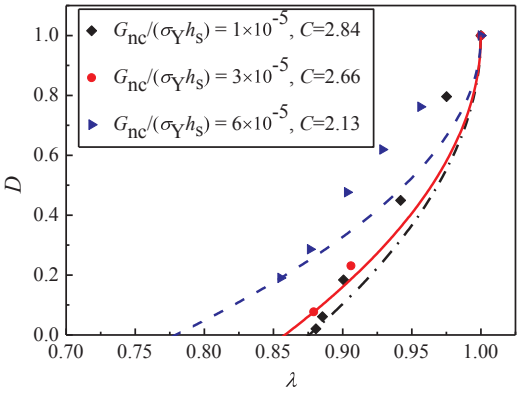

Fig. 15. Damage of two-layer systems with different interface fracture toughness and same interface strength (T_n/σ_Y = 0.4) under three-point bending loading.

Acknowledgements

This work was supported by the NSFC grants of China (Nos. 11672296, 11372318, 11432014, 11672301, 11521202), and the Strategic Priority Research Program of the Chinese Academy of Sciences (Grant No. XDB22040501).

Appendix A. Supplementary material

Supplementary data associated with this article can be found, in the online version, at http://dx.doi.org/10.1016/j.engfracmech.2018.06.040.

References

[1] Tvergaard V, Hutchinson JW. The influence of plasticity on mixed mode interface fracture. J Mech Phys Solids 1993;41:1119–35.
[2] Turon A, Camanho PP, Costa J, Davila CG. A damage model for the simulation of delamination in advanced composites under variable-mode loading. Mech Mater 2006;38:1072–89.
[3] Zhao HF, Wei YG. Determine of interface properties between micro-thick metal film and ceramic substrate using peel test. Int J Frac 2007;144:103–12.
[4] Thouless MD. Crack spacing in brittle films on elastic substrates. J Am Ceram Soc 1990;73:2144–6.
[5] McGuigan AP, Briggs GAD, Burlakov VM, Yanaka M, Tsukahara Y. An elastic–plastic shear lag model for fracture of layered coatings. Thin Solid Films 2003;424:219–23.
[6] Bialas M, Mroz Z. An energy model of segmentation cracking of thin films. Mech Mater 2007;39:845–64.
[7] Li XN, Liang LH, Xie JJ, Chen L, Wei YG. Thickness-dependent fracture characteristics of ceramic coatings bonded on the alloy substrates. Surf Coat Technol 2014;258:1039–47.
[8] Zhou M, Yao WB, Yang XS, Peng ZB, Li KK, Dai CY, et al. In-situ and real-time tests on the damage evolution and fracture of thermal barrier coatings under tension: a coupled acoustic emission and digital image correlation method. Surf Coat Technol 2014;240:40–7.
[9] Yang L, Zhou YC, Mao WG, Lu C. Real-time acoustic emission testing based on wavelet transform for the failure process of thermal barrier coatings. Appl Phys Lett 2008;93:231906.
[10] Vaunois JR, Poulain M, Kanoute P, Chaboche JL. Development of bending tests for near shear mode interfacial toughness measurement of EB-PVD thermal barrier coatings. Eng Fract Mech 2017;171:110–34.
[11] Li B, Fan XL, Okada H, Wang TJ. Mechanisms governing the failure modes of dense vertically cracked thermal barrier coatings. Eng Fract Mech 2018;189:451–80.
[12] Jiang JS, Wang WZ, Zhao XF, Liu YZ, Cao ZM, Xiao P. Numerical analyses of the residual stress and top coat cracking behavior in thermal barrier coatings under cyclic thermal loading. Eng Fract Mech 2018;196:191–205.
[13] Yang L, Zhou YC, Lu C. Damage evolution and rupture time prediction in thermal barrier coatings subjected to cyclic heating and cooling: an acoustic emission method. Acta Mater 2011;59:6519–29.
[14] Hille TS, Turteltaub S, Suiker ASJ. Oxide growth and damage evolution in thermal barrier coatings. Eng Fract Mech 2011;78:2139–52.
[15] Liu HY, Liang LH, Wang YB, Wei YG. Fracture characteristics and damage evolution of coating systems under four–point bending. Int J Appl Ceram Tec 2016;13:1043–52.
[16] Hao SW, Xia MF, Ke FJ, Bai YL. Evolution of localized damage zone in heterogeneous media. Int J Damage Mech 2010;19:787–804.
[17] Liang LH, Li XN, Liu HY, Wang YB, Wei YG. Power-law characteristics of damage and failure of ceramic coating systems under three-point bending. Surf Coat Technol 2016;285:113–9.
[18] Xu ZH, Yang Y, Huang P, Li X. Determination of interfacial properties of thermal barrier coatings by shear test and inverse finite element method. Acta Mater 2010;58:5972–9.
[19] Zotov N, Bartsch M, Eggeler G. Thermal barrier coating systems - analysis of nanoindentation curves. Surf Coat Technol 2009;203:2064–72.
[20] Barenblatt GI. The mathematical theory of equilibrium cracks in brittle fracture. In: Kerman Th, editor. Advanced in applied mechanics; 1962.
[21] Hamitouche L, Tarfaoui M, Voutrin A. An interface debonding law subject to viscous regularization for avoiding instability: application to the delamination problems. Eng Fract Mech 2008;75:3084–100.
[22] Balzani C, Wagner W. An interface element for the simulation of delamination in unidirectional fiber-reinforced composite laminates. Eng Fract Mech 2008;75:2597–615.
[23] Mi Y, Crisfield MA, Davies GAO, Hellweg HB. Progressive delamination using interface elements. J Compos Mater 1998;32:1246–72.
[24] Zhu W, Yang L, Guo JW, Zhou YC, Lu C. Numerical study on interaction of surface cracking and interfacial delamination in thermal barrier coatings under tension. Appl Surf Sci 2014;315:292–8.
[25] Liu HY, Wei YG, Liang LH, Liu XH, Wang YB, Ma HS. Damage characterization model of ceramic coating systems based on energy analysis and bending tests. Ceram Int 2018;44:4807–13.
[26] Bai YL, Bai J, Li HL, Ke FJ, Xia MF. Damage evolution, localization and failure of solids subjected to impact loading. Int J Impact Eng 2000;24:685–701.
[27] Liang LH, Wei H, Li XN, Wei YG. Size-dependent interface adhesive energy and interface strength of nanostructured systems. Surf Coat Technol 2013;236:525–30.
[28] Wang HY, Bai YL, Xia MF, Ke FJ. Microdamage evolution, energy dissipation and their trans-scale effects on macroscopic failure. Mech Mater 2006;38:57–67.